11-20-2009

Accurate Inversion of High-Resolution Snow Penetrometer Signals for Microstructural and Micromechanical Properties

Hans-Peter Marshall
Boise State University

Jerome B. Johnson
University of Alaska Fairbanks

JOURNAL OF GEOPHYSICAL RESEARCH, VOL. 114, F04016, doi:10.1029/2009JF001269, 2009

Accurate inversion of high-resolution snow penetrometer signals for microstructural and micromechanical properties

Hans-Peter Marshall[1,2] and Jerome B. Johnson[3]

Received 16 January 2009; revised 1 June 2009; accepted 7 July 2009; published 20 November 2009.

[1] Measurements of snow using a high-resolution micropenetrometer can be used to discriminate between different snow types; in lower-density snow the signal is sensitive to microstructure, and micromechanical properties can be estimated. Although a physics-based snow penetration theory was first developed almost a decade ago, since that time the majority of studies using snow micropenetrometers have focused on using direct hardness measurements in statistical relationships. We use Monte-Carlo simulations to rigorously test the existing physics-based snow micropenetration theories over a wide range of parameters. These tests revealed four major sources of error in the inversion, which are corrected in this analysis. It is shown that this improved inversion algorithm can recover micromechanical parameters in synthetic data with much greater accuracy over the entire range of micromechanical properties observed in natural snow. Detailed examples of the inversion results are shown for eight different snow types, collected in both Alaskan and alpine snowpacks. The resulting micromechanical properties are distinctly different, indicating that a snow characterization from snow micropenetrometer estimates of micromechanical properties is likely possible. Estimates of the microscale elastic modulus, microscale strength, and structural element length make sense physically when compared to the qualitative descriptions of the different snow types. Microscale strength estimates are used to estimate macroscale strength values, and results from 33 different snow samples, covering a wide range of densities and snow types, are consistent with previously reported values from macroscale tests.

Citation: Marshall, H.-P., and J. B. Johnson (2009), Accurate inversion of high-resolution snow penetrometer signals for microstructural and micromechanical properties, *J. Geophys. Res.*, *114*, F04016, doi:10.1029/2009JF001269.

1. Introduction

[2] Snow microstructure and its related physical and mechanical properties are of fundamental importance to most scientific and engineering problems dealing with snow. Due to the wide range of snow crystal types that form, depending on atmospheric conditions, and the rapid changes snow undergoes due to subsequent metamorphism after it is deposited, snow microstructure exhibits large variability in Nature. The microstructure has a great effect on the physical, mechanical and electromagnetic properties of snow. These properties cannot be accurately estimated with bulk measurements such as density. As snow density increases, due to metamorphic or compaction processes, snow properties change from those of a foam-like material at low density [e.g., *Kirchner et al.*, 2001; *Petrovic*, 2003; *Schweizer et al.*, 2003] which are structure controlled, to a porous solid at high density with properties that are controlled by density. The transition density between foam-like and porous solid-like behavior is not well defined, but is likely between 400 and 600 kg m^{-3}, based on changes in snow microstructure and mechanical properties that occur at those densities. This paper focuses on the range of snow types that are strongly affected by microstructure, which includes most seasonal snow. A different physical theory is required for high-density snow and firn, and is beyond the scope of this paper.

[3] Because snow strength depends strongly on microstructure, vertical profiles of snow grain size and shape are used operationally in avalanche forecasting. The porosity of snow is also controlled by microstructure. The vertical profile of porosity within the snowpack determines the routing of meltwater, and is an important parameter in snow hydrologic modeling. The microstructure has a dominant effect on the thermal conductivity of snow; therefore estimates are necessary for accurately modeling temperature profiles in seasonal snowpacks as well as in polar firn on the major ice sheets [*Dadic et al.*, 2008]. Microstructure controls the compressive strength of snow, and is therefore important for the mobility of animals and vehicles in snow covered areas.

[4] Possibly the most important problem in snow hydrology today is estimating the amount of water the snowpack

[1]Center for Geophysical Investigation of the Shallow Subsurface, Department of Geosciences, Boise State University, Boise, Idaho, USA.
[2]U.S. Army Cold Regions Research and Engineering Laboratory, Hanover, New Hampshire, USA.
[3]Institute of Northern Engineering, University of Alaska Fairbanks, Fairbanks, Alaska, USA.

0148-0227/09/2009JF001269$09.00

represents, or the snow water equivalent (SWE), from airborne and spaceborne platforms. Passive sensors are used operationally to estimate SWE, once calibrated for a specific region, however their spatial resolution is low (~25 km) and uncertainties are high. Active microwave radar has shown promise and has the advantage of much higher spatial resolution (~5–100 m), but is not currently used to estimate SWE. The major limitation of both active and passive microwave measurements of snow is that they are extremely sensitive to snow microstructure, which is prohibitively difficult to measure over large areas with current technology.

[5] Although characterizing snow microstructure is of the utmost importance for avalanche forecasting [e.g., *McClung and Schaerer*, 1993], remote sensing [e.g., *Rees*, 2006], snow hydrology [e.g., *Colbeck and Anderson*, 1982], engineering [e.g., *Shapiro et al.*, 1997], and even biology [e.g., *Lundmark and Ball*, 2008] in cold regions, current techniques are either qualitative or time consuming and expensive. Standard field measurements involve scraping a sample of snow from the wall of a snowpit, observing the crystals with a magnifying lens, and estimating grain size and shape. Small samples of snow (~1000 cm^3) can be preserved by filling the void space with a chemical solution such as diethl phthalate, and then later analyzed in the lab by cutting thin sections and using polarizing filters, or by photographing surface sections. These techniques are very labor intensive and time consuming, but result in accurate, detailed descriptions of snow microstructure. Recent studies have used X-ray tomography to analyze samples in the laboratory with great success [e.g., *Kaempfer and Schneebeli*, 2007; *Flin et al.*, 2003].

[6] While these laboratory techniques give very accurate microstructure information, they cannot be used in the field to measure microstructure over large areas, because they are too time consuming. Standard field observations are qualitative and observer-dependent, complicating their application in the context of modeling. A technique, which can rapidly and quantitatively measure snow microstructure is desperately needed [*Shapiro et al.*, 1997], and would have applications in all areas of snow science as microstructure is known to vary widely over short distances.

[7] The SnowMicroPenetrometer (SMP) [*Schneebeli and Johnson*, 1998; *Johnson and Schneebeli*, 1999] was recently developed to accurately measure snow layering, hardness and microstructure for snow avalanche and engineering applications. A snow penetration theory was developed to estimate microstructural and micromechanical parameters from the SMP signal [*Johnson and Schneebeli*, 1999], however most of the subsequent studies have focused on the direct snow hardness measurement [e.g., *Birkeland et al.*, 2004; *Kronholm et al.*, 2004; *Lutz et al.*, 2007; *Satyawali et al.*, 2009] and empirical relationships between hardness and other snow properties [e.g., *Schneebeli et al.*, 1999; *Pielmeier and Schneebeli*, 2003; *Pielmeier*, 2003]. While there are many SMPs currently in use by scientists around the world, a single analysis method has not become standardized, making it difficult to compare results from different studies.

[8] Below we revisit the original physics-based micromechanical theory [*Johnson and Schneebeli*, 1999] and a more recent modification to this theory [*Sturm et al.*, 2004], and test the application of this method over a wide range of microstructural parameters. We improve upon the theory by adding four important modifications, which greatly reduce errors in the inversion of the microstructural parameters when applied to simulated SMP signals. The application of this improved theory to real signals is discussed, the various methods used to remove noise in the signal are described, and example results from eight different snow types are shown in detail. The results are promising, with derived micromechanical properties that make sense when compared to the qualitative descriptions of the eight snow types. The microscale strength is used to estimate macroscale strength values for 33 different samples covering a wide range of densities. These macroscale values are shown as a function of density and compared with previous studies on macroscale samples, with good agreement. The code used for this analysis is open and freely available upon request, and it is the hope of the authors that this work will help to standardize initial SMP analysis for micromechanical properties to aid in comparing results from different independent studies.

2. Review of Previous Snow Penetration Theory

[9] We begin with a brief review of the snow penetration theory first developed by *Johnson and Schneebeli* [1999] and later modified by *Sturm et al.* [2004], as it is critical to the following description of our more recent improvements.

[10] *Johnson and Schneebeli* [1999] developed the first physics-based approach for analyzing SMP signals to determine the microstructural, micromechanical, and macroscale mechanical properties of snow. This theory of snow penetration assumes that the SMP force distance record is due to elastic deflection and brittle failure of individual snow microstructural elements, and ice/SMP friction. A microstructural element is defined as the smallest volume of ice matrix material that supports an applied load in the snow. The microstructural elements are modeled as cellular solid units, where a cell is an enclosed (or surrounded) space and a cellular solid is a cell with solid edges [*Gibson and Ashby*, 1997] made up from the ice matrix. Compaction of failed elements is taken to be negligible (reasonable for lower-density snow), and the elements are assumed to have a mean constant dimension, L, and are randomly distributed. Each element ruptures at a rupture force, f, and at a deflection length, δ, which is less than L. The three basic structural parameters that can be identified from the deformation and failure of individual elements (L, δ, f) are illustrated in Figure 1.

[11] Force spikes in the SMP record are assumed to represent the rupture of individual elements, and the vertical force distance record is first transformed to distances and forces normal to the penetrometer tip, accounting for friction between the tip and the ice matrix. The displacement, in the direction normal to the tip, $d = d_z \sin\theta$, is a function of the tip shape, where d_z is the displacement measured in the vertical direction, and θ is the half angle of the penetrometer cone tip. The total force in the direction normal to the tip, F, is

$$F = \frac{F_z}{\sin\theta + \mu\cos\theta} \tag{1}$$

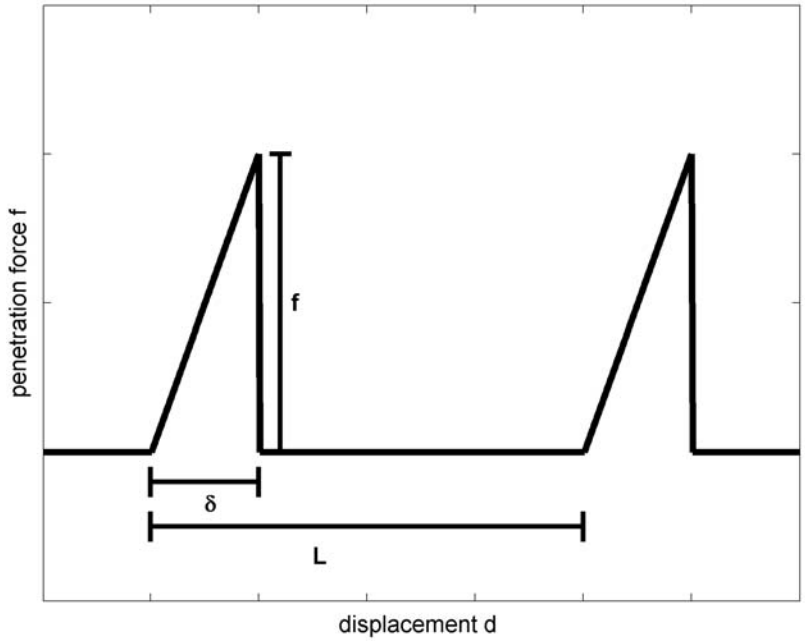

Figure 1. Structural element model and three basic parameters: the structural element length, L, the deflection at rupture, δ, and the rupture force, f.

where μ is the coefficient of friction between the penetrometer and the ice matrix, and F_z is the total force measured by the SMP in the vertical direction. These geometrical corrections to the distance and force calculate their respective component in the direction normal to the SMP tip. These corrections are performed at the beginning of the analysis; all force and distance values used in equations and discussions below imply this normal component of force and distance.

2.1. Structural Element Length

[12] The structural element length is related to the number of ruptures per mm. *Johnson and Schneebeli* [1999] first defined the structural element length assuming that each element occupies a cubical volume, $V_e = L^3$, and the total volume deformed is $V_T = Az = \pi r^2 z$, where $A = \pi r^2$ is the base area of the of the penetrometer tip. During the distance z the penetrometer records N ruptures. Assuming that each drop in the force signal represents the rupture of an individual element, we can estimate the structural element length, L, averaged over the distance z as

$$L = \sqrt[3]{\frac{V_T}{N}} = \sqrt[3]{\frac{\pi r^2 z}{N}} \tag{2}$$

Sturm et al. [2004] modified this relation by assuming that each element instead occupies a spherical volume, $V_e = \frac{4}{3}\pi r_S^3$, where the radius of the sphere, $r_S = L/2$. The structural element length in this case is

$$L = \sqrt[3]{\frac{6 r^2 z}{N}} \tag{3}$$

The two equations differ by a constant factor of $\sqrt[3]{6/\pi} = 1.24$; in the following we shall use equation (2); however, using equation (3) has little effect on the results of the following analysis. Estimating L from a penetrometer signal therefore requires only a measurement of the number of ruptures per mm.

2.2. Rupture Force

[13] One of the basic assumptions of the theory is that sharp drops in the force-distance record are the result of individual structural elements rupturing. Therefore, by locating the maxima and minima in the signal, each individual rupture force can easily be calculated. Both previous studies calculated the average rupture force over a distance z in which N ruptures occurred as

$$f = \frac{\sum_{i=1}^{N} f_i}{N} \tag{4}$$

where f_i is the rupture force for an individual element (difference in force from a local maximum to the next local minimum) calculated in the direction normal to the penetrometer tip. Noise in the SMP signal can cause fluctuations which are not caused by ruptures of individual elements – several methods have been used to remove noise, and are discussed in section 5.

2.3. Deflection at Rupture

[14] Snow behaves nearly linear elastically with brittle failure at strain rates above 10^{-3} s^{-1} [e.g., *Shapiro et al.*, 1997]. Since strain rates in snow during an SMP measurement are well above this threshold (penetration rate is 20 mm s^{-1}, strain rates are on the order of 10 s^{-1}), each element is assumed to undergo a linear elastic displacement and rupture within a distance L. *Johnson and Schneebeli* [1999] assumed that element locations can be described by a

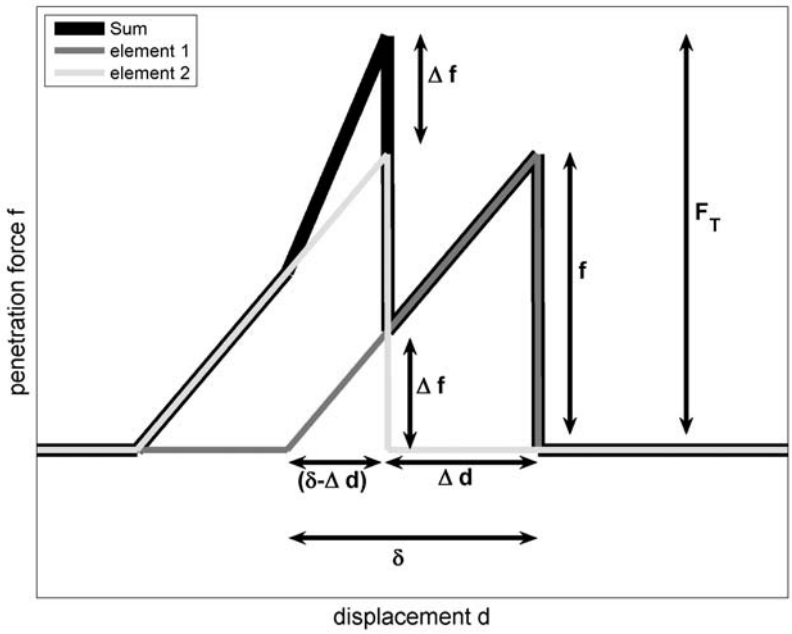

Figure 2. Two engaged structural elements and their sum. Shown are the rupture force, f, the deflection at rupture, δ, the total force at the first peak, F_T, the distance from the first peak to the second peak, Δd, and the contribution to F_T of the second element, Δf.

uniform random distribution, therefore the probability of contact of any microstructural element is

$$P_c = \frac{\delta}{L} = \frac{N_e}{N_a} \tag{5}$$

[*Gibson and Ashby*, 1997], where the number of available elements, $N_a = A/L^2$, and N_e is the number of engaged elements. When engaged, a structural element contributes to the total force by an amount between zero and f. Since element behavior is linear elastic, the average contribution of any engaged structural element is $f/2$. The mean total penetration force normal to the tip, F_m, is therefore

$$F_m = \frac{f}{2} N_e = \frac{f}{2} N_a P_c = \frac{f}{2}\left(\frac{A}{L^2}\right)\left(\frac{\delta}{L}\right) = \frac{fA\delta}{L^3} \tag{6}$$

Solving this equation for the deflection at rupture, δ, and using equation (2) we have

$$\delta = \frac{F_m}{Af} L^3 = \frac{F_m}{A}\left(\frac{N}{\sum_{i=1}^{N} f_i}\right)\left(\frac{Az}{N}\right) = \frac{F_m z}{\sum_{i=1}^{N} f_i} \tag{7}$$

This estimate of deflection at rupture, δ, does not depend on the number of measured ruptures, but only the mean total force, F_m, the penetration distance, z, and the sum of all the individual rupture forces, f_i.

[15] *Sturm et al.* [2004] removed the assumption that the individual element locations were distributed randomly by directly calculating the number of engaged elements, N_e. They calculated the contribution of each engaged element to the total peak force, F_T. Each engaged element contributes a fraction of its rupture force, proportional to the amount each element has been deflected. The total force at a given peak, F_T, is the sum of the contributions of all engaged elements, and can be expressed as

$$F_T = f + \frac{f}{\delta}(\delta - \Delta d_1) + \frac{f}{\delta}(\delta - \Delta d_2) + \cdots + \frac{f}{\delta}(\delta - \Delta d_n)$$
$$F_T = f \sum_{i=0}^{N_e}\left(1 - \frac{\Delta d_i}{\delta}\right) \tag{8}$$

where Δd_i is the distance from the current peak to the rupture of the i^{th} element, $\delta - \Delta d_i$ is the current deflection of the i^{th} engaged element, and $\Delta d_0 = 0$. An example with $N_e = 2$ is shown in Figure 2. The deflection at rupture, δ, and the number of engaged elements, N_e, are initially unknown. The right-hand side of equation (8) is calculated iteratively, assuming $\delta = \Delta d_{n+1}$ and increasing N_e, until the calculated total peak force exceeds the measured total peak force. When this condition is reached, N_e is known and

$$\delta = \Delta d_{N_e+1} \tag{9}$$

2.4. Derived Micromechanical Parameters

[16] From these three basic microstructural parameters, *Johnson and Schneebeli* [1999] derived several micromechanical parameters. Assuming linear elastic behavior with brittle failure and no plastic deformation, calculated from zero load and displacement, the coefficient of elasticity, or the stiffness, is

$$k = \frac{f}{\delta} \tag{10}$$

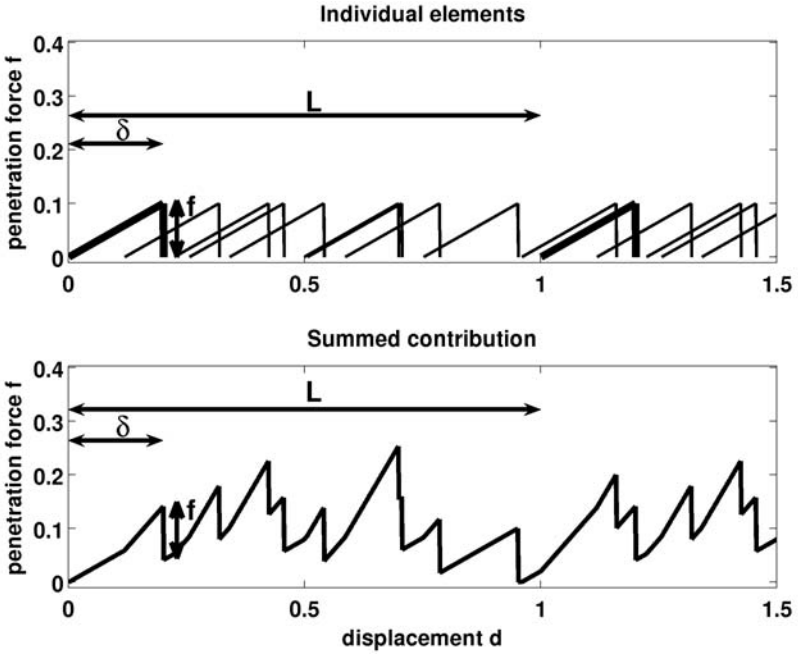

Figure 3. (top) Many structural elements and (bottom) their summed contribution. The three basic parameters are shown for the first element with the thick line in the top.

The microscale elastic modulus can be calculated as

$$E_{micro} = \frac{k}{L} = \frac{f}{\delta L} \tag{11}$$

and the microscale strength is defined as

$$\sigma_{micro} = \frac{f}{L^2} \tag{12}$$

These microscale quantities are associated with the individual structural elements of the foam-like material, and are not continuum-scale properties [e.g., *Nemat-Nasser and Hori*, 1999]. In section 6.3 we estimate the macroscale (continuum scale) strength from the microscale strength; estimating the macroscale elastic modulus from SMP measurements will be the subject of future work. Since these microscale parameters are calculated directly from the basic microstructural parameters, errors in the basic parameters can cause even larger errors in the micromechanical parameters; therefore it is important that the calculation of the basic microstructural parameters is accurate.

2.5. Accuracy of Previous Inversions

[17] *Johnson and Schneebeli* [1999] performed Monte Carlo simulations using their theory of penetration and found good agreement with measurements of zirconia foam [*Gibson and Ashby*, 1997], indicating their assumptions may be appropriate. They created simulated SMP signals by adding together individual structural elements with constant microstructural parameters: $L = 1$ mm, $f = 0.1$ N, and $\delta = 0.2$ mm, and three different values of the number of available elements, $N_a = A/L^2 = 1$, 10, and 25. The element locations were chosen from a uniform random distribution, and the simulated signal was generated by summing the contribution of all elements. One example Monte-Carlo realization for $N_a = 10$ is shown in Figure 3, with the individual elements on the top and the simulated signal on the bottom. The three basic parameters are indicated for the structural element shown with the thick line in the top.

[18] The analysis described above was applied to simulated signals, and the results were compared to the microstructural values used to generate the simulation. They state that for $N_a = 1$ the parameters were recovered exactly, for $N_a = 10$ the error was about 5%, and for $N_a = 25$ the error was about 10%. *Kronholm* [2004] states that Monte-Carlo simulations were used to test the accuracy of recovery and that f and L (using equations (2) and (4)) had an error of less than 0.01%, however the values of the parameters used in the simulations were not given.

3. Improvements

[19] The error in the recovery of microstructural parameters increases rapidly as the number of available elements, N_a, increases, since many elements are in contact with the SMP tip at a given time. It is therefore important to test the accuracy of recovery throughout the observable range of parameters, especially at higher values of N_a, using the actual measurement parameters of the SMP.

[20] *Marshall* [2005] used Monte-Carlo simulations for $N_a = 25$, $L = 1$ mm, $\delta = 0.2$ mm, and $f = 0.1$ N, following *Johnson and Schneebeli* [1999], in an attempt at finding the causes of error in the recovery of the parameters. He suggested improvements to the analysis, and below we further develop these ideas and test them over a wide range of structural element sizes. The errors become very significant for large values of N_a (small L), within the range commonly observed in snow. These errors become even more pronounced when the derived micromechanical parameters are calculated, since they depend on the basic

microstructural parameters L, f, and δ. It is therefore critical to minimize these errors for accurate inversion.

[21] After much trial and error, the four major modifications that significantly reduced the error in the recovery of the basic microstructural parameters were (1) accounting for simultaneous ruptures, (2) solving for deflection at rupture exactly, (3) using individual rupture forces when calculating deflection at rupture, and (4) correcting rupture forces for force increases during rupture events. Each of these modifications affects the accuracy of the retrieval of the three microstructural parameters in different ways, and all modifications are necessary for accurate retrieval of all three parameters. The modifications are discussed in detail in sections 3.1–3.4, and their effect on the retrieval accuracy is discussed in section 4.

3.1. Account for Simultaneous Ruptures

[22] *Marshall* [2005] found that the major cause of error was due to more than one element rupturing at once, which is a violation of one of the basic assumptions of the analysis. This caused an underestimate of the number of ruptures, N, which led to an overestimate of the structural element length, L, (see equation (2)) and an overestimate of the mean rupture force, f, (see equation (4)). These simultaneous ruptures were common over a wide range of the observed values of L in snow, when the actual sample frequency, F_s, of the SMP was used in the simulations. Since the calculation of the deflection at rupture, δ, using the *Johnson and Schneebeli* [1999] method involves the sum of all the rupture forces, $\sum f_i$, but not the mean rupture force $\overline{f}$, (see equation (7)) the deflection at rupture, δ, was not sensitive to simultaneous ruptures. The calculation of the deflection at rupture, δ, using the *Sturm et al.* [2004] method (equation (9)), however, does depend on the mean rupture force, $\overline{f}$, and therefore an overestimate in f caused an underestimate in δ. The number of simultaneous ruptures depends strongly on the sample frequency, F_s, of the SMP, the area of the SMP tip, A, and the structural element length, L.

[23] *Marshall* [2005] developed a method for accounting for simultaneous ruptures, which used a theoretical estimate of the probability that two elements would overlap. Since simultaneous ruptures always cause an increase in the calculated value of individual rupture forces, the theoretical estimate was used to adjust the largest rupture forces, assuming that they were caused by simultaneous ruptures. For the Monte-Carlo simulations involving the constant microstructural parameters above, this method corrected the errors caused by simultaneous ruptures. However, when the microstructural parameters were varied within the simulation, this method did not work properly. In addition, for smaller values of L, the probability of an overlap occurring became extremely large and, again, the method was no longer valid.

[24] In the present analysis we instead used Monte-Carlo simulations to directly predict the number of simultaneous ruptures, as a function of L. The base area of the penetrometer tip was fixed at the value for the current SMP ($A = \pi r^2 = 19.6$ mm^2); the deflection at rupture, $\delta = 0.2$ mm, and the mean rupture force, $f = 0.1$ N, were held constant. The SMP sample frequency, $F_s = 250$ samples mm^{-1}, was used. The number of measured ruptures, as a function of L, was calculated for $0.3 \leq L \leq 3$ mm. For each value of L, in steps of 0.01 mm, a 10-m Monte-Carlo simulated SMP signal was generated, containing 2,500,000 simulated force measurements. This signal was analyzed in both 1-mm and 10-mm segments, and the distribution of measured ruptures was recorded.

[25] The number of measured ruptures per mm N_m as a function L is shown in Figure 4. The shaded areas show the 95% confidence intervals for analyzing both 1-mm and 10-mm segments. The error in the calculated L (see equation (2)) becomes large as the structural element size decreases, and is much less when a 10-mm sample is analyzed compared to a 1-mm sample.

[26] These simulation data were smoothed using a weighted moving window with a normal kernel and a window width of 0.1 mm. To account for multiple ruptures in a measured SMP signal, the number of measured ruptures per mm, N_m, was first calculated. The smoothed simulation data were next interpolated at N_m using a cubic spline and the structural element size, with confidence intervals, $L(N_m) \pm \Delta L(N_m)$, was estimated. Finally, the true total number of ruptures in the penetration distance z was calculated as in equation (2):

$$N_T = \frac{Az}{L^3} \tag{13}$$

This true value of the number of ruptures was used instead of the measured number of ruptures, N, to calculate the mean rupture force

$$f = \frac{\sum_{i=1}^{N} f_i}{N_T} \tag{14}$$

as well as the deflection at rupture, $\delta(f, F_T)$, using equation (9).

3.2. Solve Exactly for Deflection at Rupture

[27] In the *Sturm et al.* [2004] approach, the total penetration peak force was calculated iteratively, until it exceeded the measured total force, at which point the deflection at rupture, $\delta = \Delta d_{n+1}$ (equation (9)), was chosen. The actual value of δ is between Δd_n and Δd_{n+1}, and can be calculated exactly. Assuming that f is constant, the deflection at rupture can be calculated as

$$\delta = \frac{\sum_{i=1}^{N_e} \Delta d_i}{N_e - \frac{F_T}{f}} \tag{15}$$

after the number of engaged elements, N_e, is found from the iterative calculation. This correction is negligible when there are many engaged elements (small L), however it becomes very important for coarse-grained snow when there are fewer engaged elements (large L).

3.3. Use Individual Rupture Forces to Calculate Deflection At Rupture

[28] Since the assumption of constant microstructural and micromechanical parameters is clearly unrealistic for snow,

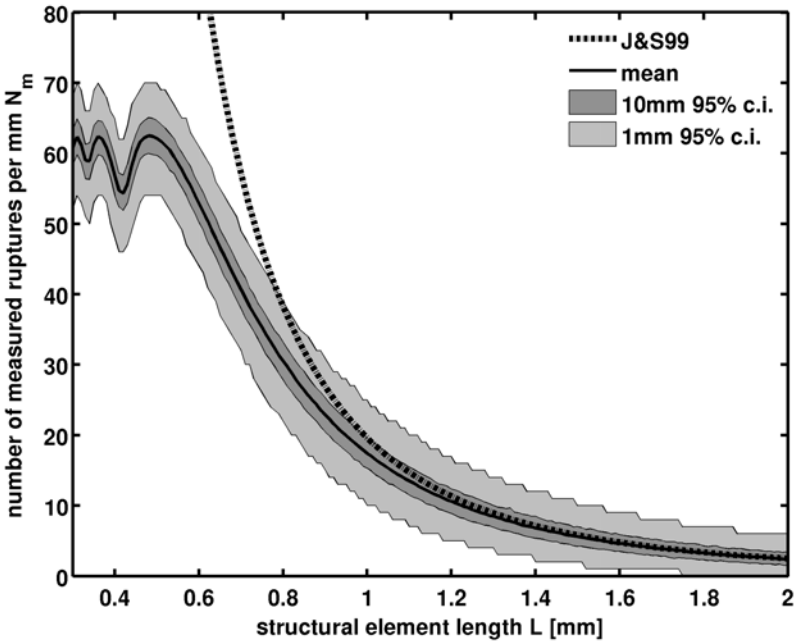

Figure 4. Number of measured ruptures per mm, N_m, as a function of input structural element length, L. Shown are the ranges of measured ruptures from Monte-Carlo simulations of 2,500,000 force measurements, at each value of L, for both 10-mm (dark gray) and 1-mm (light gray) samples, as well as equation (2) from *Johnson and Schneebeli* [1999] (dashed line).

we further modified the theory to remove the restriction that f is constant by rewriting equation (8) as

$$F_T = f_0 + f_1\left(1 - \frac{\Delta d_1}{\delta}\right) + f_2\left(1 - \frac{\Delta d_2}{\delta}\right) + \ldots + f_{N_e}\left(1 - \frac{\Delta d_{N_e}}{\delta}\right) \tag{16}$$

where each individual rupture force, rather than the mean rupture force, is used to calculate the total peak force. The equation for deflection at rupture, δ, then becomes

$$\delta = \frac{\sum_{i=1}^{N_e} f_i \Delta d_i}{\sum_{i=0}^{N_e} f_i - F_T} \tag{17}$$

If f varies substantially, as occurs in natural snow with distributions of microstructural parameters [e.g., *Kaempfer and Schneebeli*, 2007], this modification to the theory becomes important. In addition, this calculation of deflection at rupture does not depend on the total number of measured ruptures, N_m, only on the sum of the individual ruptures. Therefore improvements (sections 4.2 and 4.3) make the calculation of deflection at rupture, δ, insensitive to simultaneous ruptures, which was the major source of error.

3.4. Correct Rupture Force Digitization Error During Rupture

[29] When simultaneous ruptures do not occur, the value of f is still underestimated. This occurs because when multiple elements are engaged, a drop in force from a rupture occurs simultaneously with an increase in force due to the deformation of the other engaged elements, reducing the overall force drop. To correct for this, we used the slope of the force curve immediately after the rupture to estimate the increase in force caused by the other elements' increased deformation during the element rupture event:

$$f_i = f_i + \frac{\partial F}{\partial z}\Delta z \tag{18}$$

where $\partial F/\partial z$ is the slope of the force-distance record immediately after the i^{th} rupture, and Δz is the distance traveled during the rupture. This modification is trivial when there are few elements engaged, but becomes important when N_e is large (small L).

4. Accuracy of Inversion Applied to Simulated Signals

[30] Because the accuracy of retrieval of microstructural parameters depends strongly on the structural element length, L, we performed extensive Monte-Carlo simulations over a wide range of values of this parameter. A 1-m long simulated SMP signal, composed of 250,000 force measurements, was created using constant parameters (δ = 0.2 mm, f = 0.1 N) covering the range of structural element lengths we have measured in natural snow ($0.59 \leq L \leq 2.5$ mm). For structural element lengths less than 0.59, inverting for a unique value of L is not possible (see Figure 4), due to the sample rate of the SMP (250 samples mm^{-1}). We therefore did not attempt to simulate signals with L less than 0.59 since it is clear that we would not be able to invert such a signal uniquely. The signals were analyzed in 10-mm sections for a total of 100 independent subsamples for each

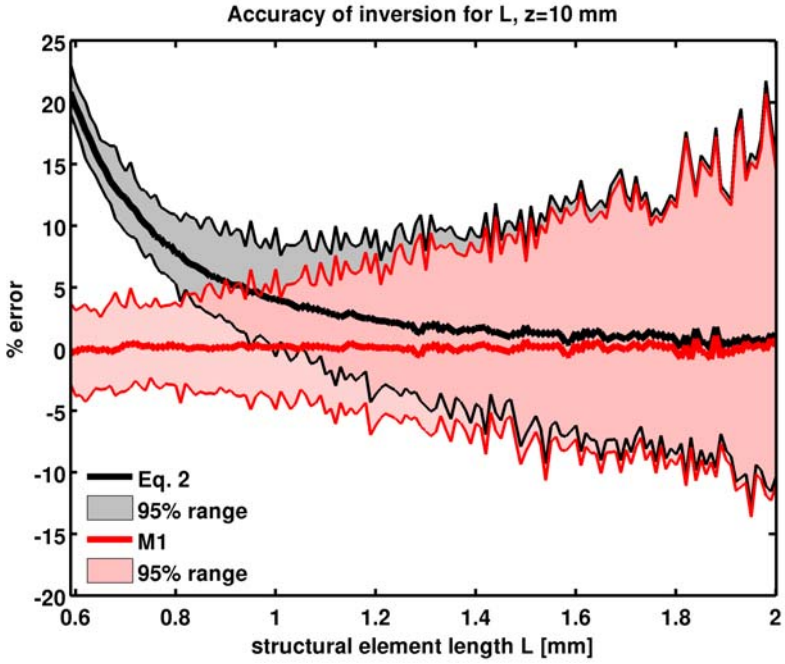

Figure 5. Accuracy of inversion for structural element length, L, as a function of input value of L. One hundred Monte-Carlo simulations of 10-mm signals were performed for each value of L. The black line shows the median result of equation (2), and the red line shows the median when simultaneous ruptures are taken into account (M1). The shaded areas show the 95% range over all simulations.

value of L. Below we describe the effect of each of the above modifications on the accuracy of the retrieval of each basic microstructural parameter. In the section 4.4, we further explore the parameter space by testing the accuracy of retrieval over the range of all three basic parameters (δ, f, L) observed in natural snow.

4.1. Structural Element Length Retrieval

[31] For an element rupture to be captured in an SMP signal, a minimum of four force measurements are required, to define the rupture force: in addition to the measurement at the local maximum and the local minimum, a measurement before the maximum and after the minimum is required in order for a local maximum and local minimum to be defined. The maximum number of ruptures that can be measured in 1 mm is approximately $F_s/4 \approx 63$ (Figure 4); there is a lower limit of $L \approx 0.59$ mm below which the structural element length can no longer be uniquely estimated. This limitation is due to the sample frequency, however does not depend on the cone diameter. Changing the cone diameter would change the likelihood of simultaneous ruptures shown in Figure 4, but not the lower limit of measurable values of L. In order to decrease this lower limit, the sample frequency would need to be increased. The uncertainty in the estimate of L also increases at large values of structural element length, due to the slope of the curve in Figure 4. At large values of L, where the number of elements is very small, a small uncertainty in the total number of elements per mm corresponds to a large uncertainty in L.

[32] The percent error in the retrieval of the structural element length as a function of the structural element length is shown in Figure 5. The black line shows the median error when equation (2) is applied, and the gray shaded region indicates the 95% range, over all 100 Monte-Carlo simulations at each value of L. This estimate is biased and overestimates the value of L for small structural element lengths, due to simultaneous ruptures. Using the previous estimate for L (equation (2)) causes an average overestimate of more than 20% for $L = 0.6$ mm, decreasing to 5% for $L = 1.0$ mm. The 95% range increases with increasing L as the structural element length approaches the subsample size.

[33] The red line shows the median error when simultaneous ruptures are accounted for, as described in section 3.1, and the red shaded region shows the 95% range over all the simulations. The median error is less than 1% over the entire range of values of L, and the 95% range coincides with the uncertainty estimated from Figure 4. This variation is caused by true variation in the number of measured ruptures for a 10-mm sample, and could only be reduced by analyzing longer signals; the variation would be more than twice as large for a 1-mm sample analyzed rather than a 10-mm sample. This improvement becomes even more important when the derived micromechanical properties are calculated; in particular the microscale strength depends strongly on L (equation (12)). For example, for $f = 0.1$ N and $L = 0.75$ mm, without modification 1 (M1), L is overestimated by 10%, causing an underestimate in σ_{micro} of more than 18%. Modifications 2–4 (M2–M4) do not have an effect on the structural element length.

4.2. Rupture Force Retrieval

[34] Simultaneous ruptures, which appear as one large rupture in the SMP signal, cause an overestimate in the mean rupture force f. The mean rupture force is sensitive to simultaneous ruptures, since f is proportional to N^{-1}. Figure 6

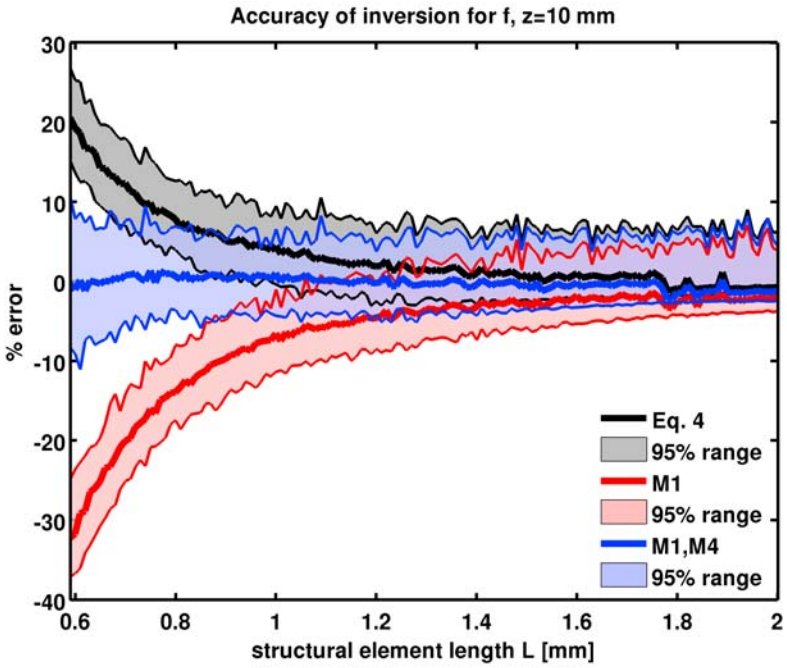

Figure 6. Accuracy of inversion for rupture force, f, as a function of input value of L. The black line shows the median using equation (4), the red line shows the median accounting for simultaneous ruptures (M1), and the blue line shows the median using M1 and accounting for digitization errors (M4). The shaded areas show the 95% range over all simulations.

shows the percent error in the inversion for rupture force, as a function of structural element length.

[35] The black line shows the median error when equation (4) is applied and the shaded gray region indicates the 95% range over all 100 Monte-Carlo simulations at each value of L. This estimate is biased and overestimates the value of f, due to simultaneous ruptures. The 95% range is not sensitive to the value of L.

[36] The red line shows the median error when simultaneous ruptures are accounted for (M1, section 3.1), and the red shaded region shows the 95% range over all the simulations. When this modification is applied, the rupture force is underestimated, by as much as 30%, for small values of L. The blue line and shaded region shows the median and 95% range when both simultaneous ruptures are accounted for and f is corrected for digitization errors (M1 and M4). The resulting estimate is now unbiased, with a median value that is less than 2% over the entire range of values of L. Both of these modifications are necessary for accurate inversion of rupture force. The 95% range is less than 10% and is caused by true variations in the number of measured ruptures in the 10-mm subsamples, and would decrease with longer subsamples. Modifications M2 and M3 do not have an effect on the rupture force.

4.3. Deflection at Rupture Retrieval

[37] The original calculation of deflection at rupture (equation (7)) is not sensitive to multiple ruptures, since it depends only on the mean total penetration force and the sum of all the individual ruptures. However, for small values of L when there are many elements engaged, the retrieval error is large due to errors caused by digitization.

[38] Figure 7 shows the percent error in the inversion for deflection at rupture, as a function of L. The black line and gray shaded region show the median error and 95% range when equation (7) is applied, over all simulations. This overestimates δ by almost 50% for $L = 0.6$ mm, decreasing to 10% at $L = 1$ mm. For $L > 1.3$ mm, there are few elements engaged at once, and the error is less than 5%. The 95% range increases slightly with increasing L, due to variations in the number of ruptures in the 10 mm subsamples.

[39] The red line and shaded region show the error in the inversion for δ when equation (9) is used, as in the work by *Sturm et al.* [2004]. This causes an error of almost 50% for $L = 0.6$ mm, overestimates δ over the entire range of L by at least 20%, and the variation increases with increasing L. The blue line and shaded region shows the error in the result for equation (9), modified to calculate δ exactly (M2, section 3.2), and when the individual rupture forces are used in the calculation (M3, section 3.3). This greatly improves the accuracy, especially at large values of L, however the accuracy is still poor for small values of L, and is worse than equation (7) for large values of L.

[40] The green line and shaded region shows the result for equation (9), with M2 and M3 applied, and in addition the rupture forces are corrected for digitization errors (M4, section 3.4). This results in a very accurate retrieval for δ, which is less than 2% over the entire range of L. In addition, the variation over the 100 Monte-Carlo simulations is less than ±0.5%, making the estimate very robust, as it does not depend on the number of measured ruptures.

[41] For comparison, the yellow line and shaded region shows the error in δ with M4 applied. This estimate is also very accurate, with a median error of less than 2% over the entire range of L. The variation is much larger (>5%) than

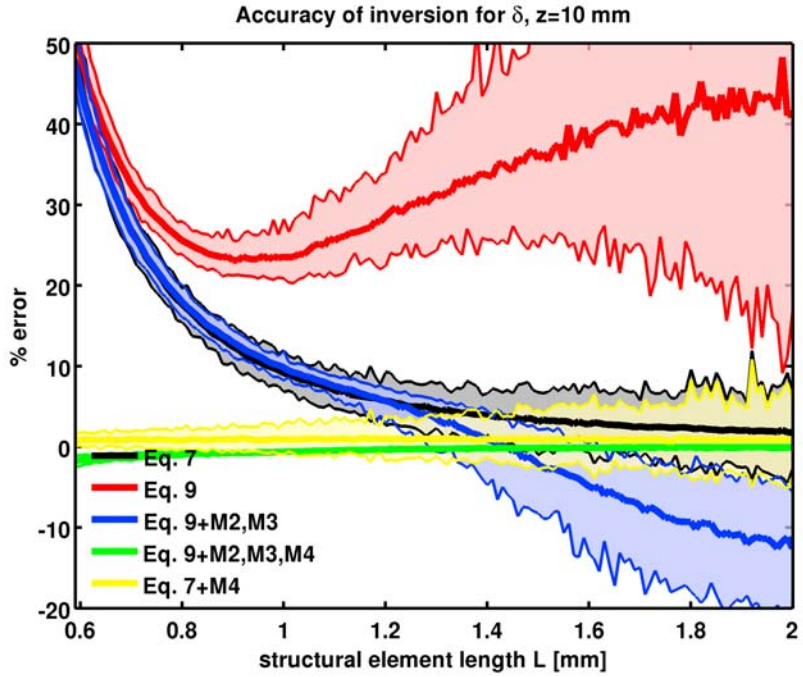

Figure 7. Accuracy of inversion for deflection at rupture, δ, as a function of input value of L. The black line shows the median using equation (7), the red line shows the results from using equation (9), and the blue line shows the results from equation (9) when δ is solved for exactly (M2) and all rupture forces are used (M3). The green line shows the results when M2, M3, and M4 are applied, and the results of equation (7) using M4 are shown in yellow. The shaded areas show the 95% range over all simulations.

equation (9) using M2–4, for $L > 1.5$ mm, therefore using equation (9) with M2, M3, and M4 is preferred.

4.4. Accuracy Over Range of All Three Parameters

[42] Although the accuracy of the inversion is most sensitive to the structural element length, we investigated the error for a range of all three microstructural parameters, using all four modifications above. Using the range of values found in natural snow, we performed Monte-Carlo simulations for a range of values of structural element length ($0.6 \leq L \leq 1.5$ mm), rupture force ($0.05 \leq f \leq 0.45$N), and deflection at rupture ($0.05 \leq \delta \leq 0.75$ mm). For every possible combination of values, we again simulated a 1-m SMP signal, and applied the inversion algorithm to the 100 independent 10-mm subsamples. A total of 400 independent combinations were tested, covering the range of observed values in natural snow, with 100 independent simulated signals analyzed for each combination.

[43] The accuracy of the inversion for both rupture force, f, and structural element length, L, did not change for different input values of f and δ. The accuracy was only sensitive to the input value of L. Figure 8 shows box plots indicating the range of errors from all 40,000 Monte-Carlo simulations for L (Figure 8, top) and f (Figure 8, bottom), as a function of L. The mean error was always very close to zero for all combinations, demonstrating that the inversion algorithm is unbiased. The upper plot shows the error in inverting for L and the lower plot shows the error in inverting for f.

[44] The 95% range of the error in L increases from 5% at $L = 0.6$ mm to 10% at $L = 1.5$, due to variations in the true number of ruptures in a 10-mm subsample. Estimates have an error less than 3% for all combinations of parameters 50% of the time, and the median error is always less than 0.5%. The 95% range in the error in f decreases from 12% at $L = 0.6$ mm to 6% at $L = 1.5$ mm as the inversion for f is most accurate for this parameter when fewer elements are engaged. The middle 50% of the data show an error of less than 4% over all combinations, and the median error is always less than 1%.

[45] The accuracy of the inversion for deflection at rupture, δ, was insensitive to changes in rupture force, f, but was sensitive to the input values of L and δ. Figure 9 shows box plots indicating the range of error in δ from all 40,000 Monte-Carlo simulations, as a function of δ (Figure 9, top) and L (Figure 9, bottom). 95% of the time the error in estimating δ is less than 3%, with the exception of when δ is very small ($\sim$0.05 mm) for which the 95% accuracy is less than 8%. The median values are always within 2% with a very slight negative bias which decreases to less than 0.5% for $\delta > 0.15$ mm and $L > 0.7$ mm. Over the entire parameter space our current inversion algorithm is very accurate, and these error estimates can be used to assign an uncertainty to the inversion results based on the values of the three basic parameters.

5. Inversion of SMP Measurements of Natural Snow

[46] Actual SMP measurements in natural snow include variations in the force distance record caused by noise, which must be removed before applying the inversion algorithm described above. Although the resolution of the force sensor is 0.001 N, measurements in air show fluctua-

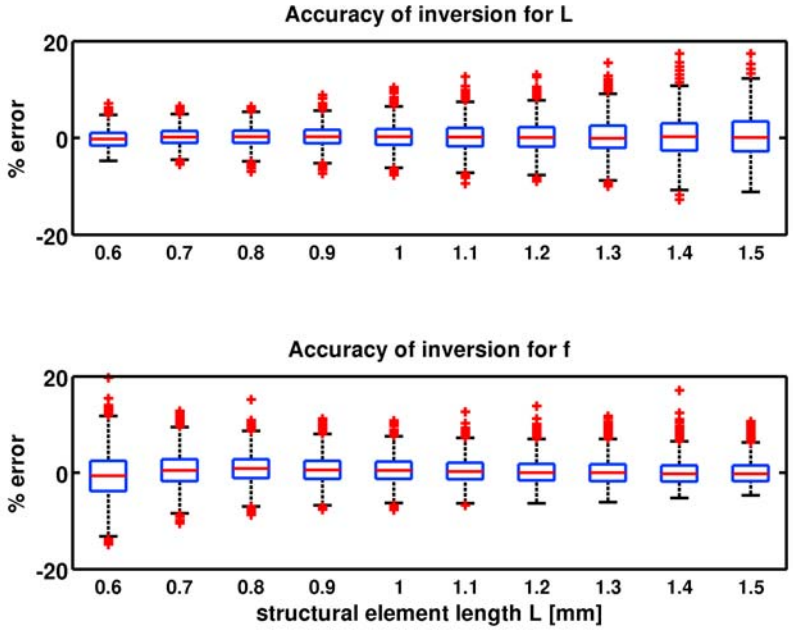

Figure 8. Accuracy of inversion for (top) structural element length, L, and (bottom) rupture force, f, as a function of input value of L. Box plots show the range over 40,000 Monte-Carlo simulations covering the range of observed values of all three basic microstructural parameters. The box shows the middle 50% of the data, the whiskers show 95%, and the plus symbols are outliers.

tions on the order of 0.01 N. It is possible that once the SMP rod is in the snowpack, vibrations of the rod are dampened, however force spikes caused by effects other than ruptures of structural elements may also increase with increasing maximal penetration force. Several different methods have been used to remove unwanted fluctuations in the signal, described below.

[47] *Johnson and Schneebeli* [1999] located all of the maxima and minima in the signal, used these to calculate rupture forces, and removed all ruptures with a value of f_i

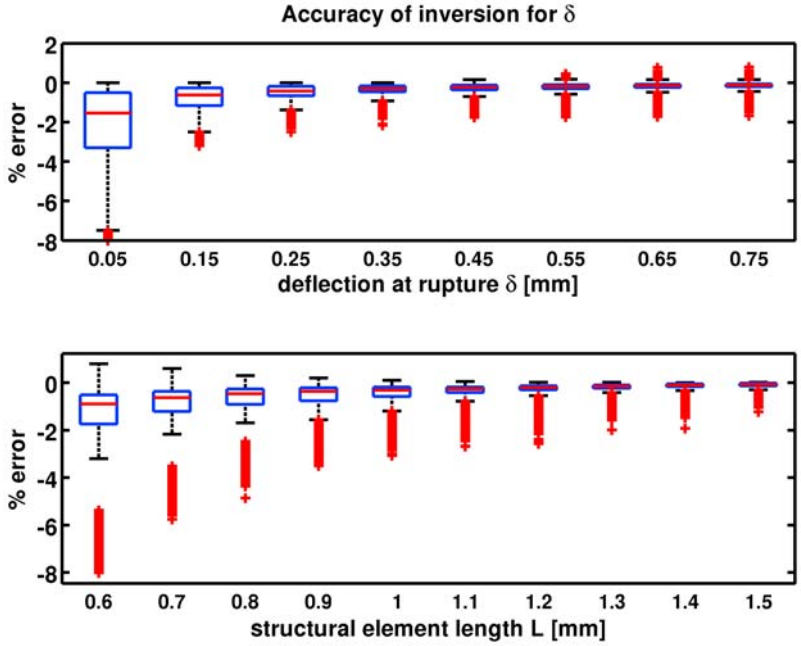

Figure 9. Accuracy of inversion for deflection at rupture, δ, as a function of (top) input value of δ and (bottom) input value of L. Box plots show the range over 40,000 Monte-Carlo simulations covering the range of observed values of all three basic microstructural parameters. The box shows the middle 50% of the data, the whiskers show 95%, and the plus symbols are outliers.

Table 1. Description of Eight Snow Samples

Sample	Snowpack	ICSSG Code	Description	Density (kg/m^3)	Grain Size (mm)
A1	Alaskan	RGlr	Large rounded particles	229	0.6
A2	Alaskan	MFcr(DH)	Refrozen depth hoar	280	1.2
A3	Alaskan	DHch	Depth hoar/chains	238	1.2
A4	Alaskan	RGwp	Rounded grains/wind packed (slab)	400	0.4
B1	alpine	PPsd	Precipitation particles/ stellars/dendrites	210	0.5–1
B2	alpine	RGlr	Large rounded particles	275	1
B3	alpine	DHpr	Depth hoar/hollow prisms	325	1–2
B4	alpine	IFsc	Ice formation/sun crust	400	1–2

less than a certain threshold. The threshold was chosen based on SMP measurements in air. *Kronholm* [2004] used a rupture slope threshold method, in which the slope of the SMP signal during a rupture had to exceed some minimum slope requirement. He investigated the sensitivity of the macroscale elastic modulus estimate to the rupture force threshold, and found that the sensitivity depended on snow type. He presented results from two different snow types and found that a rupture slope of -0.45 N mm^{-1} gave the results with the least variance. He used this threshold in subsequent calculations, but stated that effect of the choice of rupture slope threshold required further investigation.

[48] *Sturm et al.* [2004] first removed a linear trend in the SMP signal, which they assumed was caused by static electric charge buildup in the load sensor's charge amplifier. For large penetration forces, a high-frequency, low-amplitude chatter was observed which was removed with a binomial smoothing filter. Finally, a cubic spline was fit to the detrended, filtered SMP signal, and subtracted. The remaining residual signal was used to locate force ruptures, and all of these ruptures were used. This may be the reason this study found structural element length values much less than those found in the *Johnson and Schneebeli* [1999] study, both of which used Alaskan snow. The different noise removal approaches [*Johnson and Schneebeli*, 1999; *Sturm et al.*, 2004; *Kronholm*, 2004] all have different effects on the results, making comparisons between studies impossible, highlighting the need for an improved inversion method that can be used to standardize SMP analysis methodology.

6. Application of Improved Inversion to Eight Snow Types

[49] To illustrate the results of the inversion procedure described in this paper, below we show detailed examples of eight distinctly different snow types, from both Alaskan and alpine environments. Four of these snow samples were from the same measurements used by *Johnson and Schneebeli* [1999], and four were from an alpine snowpack. Table 1 lists all eight snow types, their class and subclass according to the International Classification for Seasonal Snow on the Ground [*Fierz et al.*, 2009], density, and grain size.

[50] A 10-mm section was chosen from the center of each sample, and these force records are shown on a semilog scale in Figure 10. The force values cover several orders of magnitude, and have different variances and frequencies in these distinctly different types of snow. Within each snow type the signal characteristics are consistent over the entire 10-mm sample.

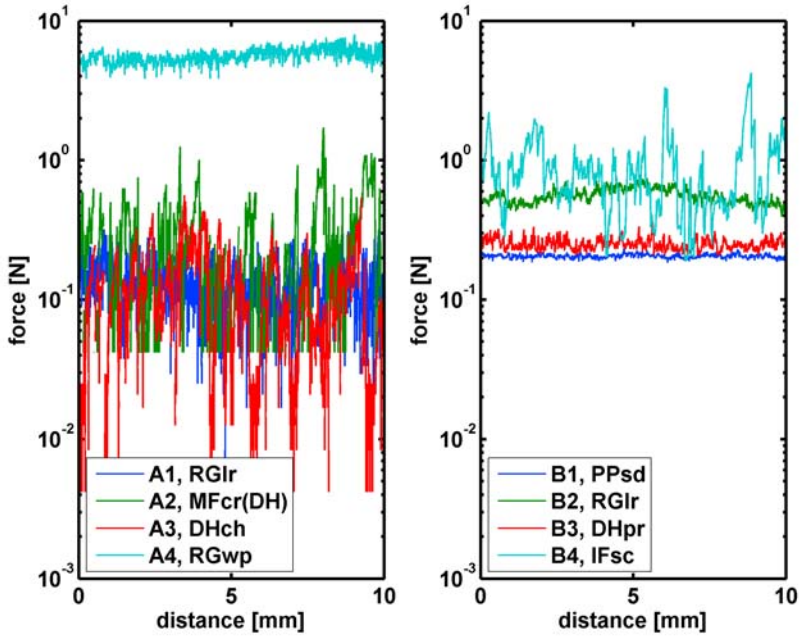

Figure 10. Force distance record from eight different snow types: (left) four from Alaska and (right) four from an alpine snowpack on a semilog scale. Force values cover 3 orders of magnitude. Each snow type has a very different magnitude, variance, and frequency, but within each snow type these signal characteristics are consistent along the entire 10-mm sample (2500 measurements). The legend shows the sample label, class, and subclass corresponding to Table 1.

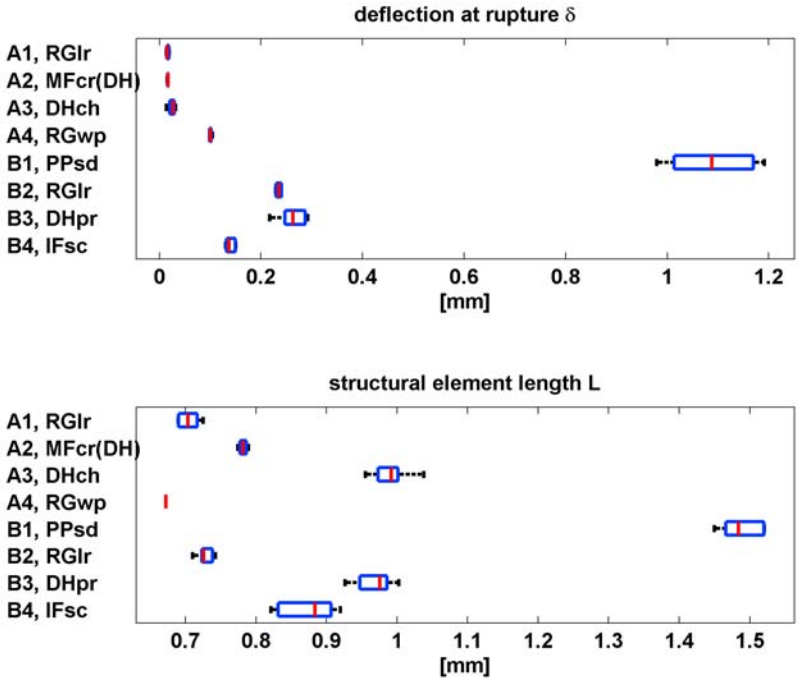

Figure 11. Box plots of (top) deflection at rupture, δ, and (bottom) structural element length, L, for all eight snow samples. Details of each snow type are given in Table 1. The box shows the middle 50% of the data, the whiskers show 95%, and the plus symbols are outliers.

[51] The legend indicates the snow sample label, and the class and subclass code, corresponding to Table 1. *Johnson and Schneebeli* [1999] used the following four-letter abbreviations for their four snow samples, based on the location of the sample and a description of the snow type: sample A1 is Glass Park equilibrium (GPEQ), sample A2 is Valdez refrozen depth hoar (VDH), sample A3 is Glass Park depth hoar (GPDH), and sample A4 is Rainbow Mountain wind slab (RMWS). Sample A4 was shown to have a periodic signal [*Pielmeier*, 1998], possibly caused by a stick-slip mechanism, therefore results for this snow sample should be interpreted with caution.

6.1. Basic Microstructural Parameters

[52] Using the inversion algorithm described above, basic microstructural parameters were calculated for all eight snow types. A rupture force threshold of 0.0165 N, normal to the tip, was used, based on the fluctuations of the SMP signal in air. Since each sample was only 10-mm long, each sample was subdivided into 6 overlapping 5-mm subsections. The deflection at rupture, δ, (Figure 11, top) and structural element length, L, (Figure 11, bottom) are shown for the eight snow types as box plots. The values of deflection at rupture are significantly different for almost all eight snow types, and the new snow (sample B1) shows the largest value, as expected.

[53] The structural element length, L, can be interpreted as the mean distance between bonds. The precipitation particles (sample B1) have the largest value of L as expected, since this new snow sample has had little time to sinter and therefore likely has few bonds. The depth hoar samples (A3 and B3) have the next largest structural element length, which also makes sense as this type of snow is characterized by large grains with few bonds. The depth hoar sample that has undergone a melt freeze cycle (sample A2) and the sun crust (sample B4) have lower values of L, likely due to bonds formed from refrozen liquid water, followed by the two rounded grain samples (A1 and B2), which agree with the qualitative description of rounded grains typically having many bonds. The smallest value of L occurs in the wind packed rounded grains, which also makes sense, since the wind causes the snow to become very closely packed allowing many bonds to form. All eight snow types have distributions of L that are different and do not overlap. Without the modifications described above, the smaller L values would be overestimated, causing all values to be much closer in magnitude, and this parameter would not be nearly as useful for classifying snow type.

[54] Figure 12 shows the rupture force, f, (Figure 12, top) and strain at failure,

$$\varepsilon_f = \frac{\delta}{L},$$

(Figure 12, bottom) for the eight snow types. For the Alaskan samples the wind packed snow (A4) has the largest rupture force, followed by the refrozen depth hoar (A2), with the smallest values of f for the depth hoar (A3) and rounded grains (A1). In the alpine samples, the sun crust (B4) shows the largest rupture forces, with smaller values for the rounded grains (B2) and depth hoar (B3), and the smallest rupture force values for the precipitation particles (B1), as expected.

[55] The values of all three basic parameters are well separated, and vary with different trends for each parameter. This indicates that it should be possible to develop a snow

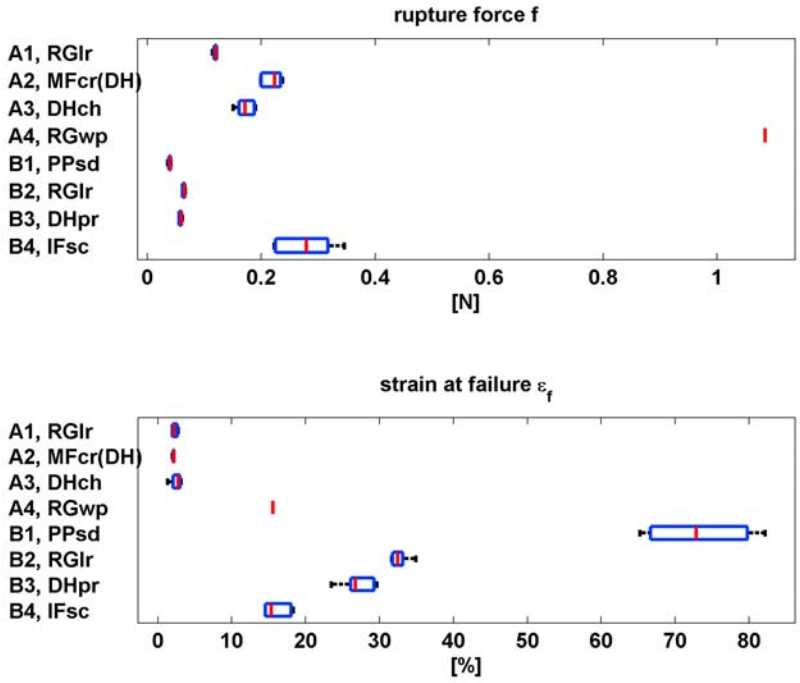

Figure 12. Box plots of (top) rupture force, f, and (bottom) strain at failure, ε_f, for all eight snow samples. Details of each snow type are given in Table 1. The box shows the middle 50% of the data, the whiskers show 95%, and the plus symbols are outliers.

characterization index from these basic microstructural parameters, although this is beyond the scope of this paper. By standardizing the inversion algorithm, results from different studies can be directly compared, which will hopefully lead to such a characterization. A recent study has shown promising preliminary results for a snow characterization using basic statistics of the SMP hardness measurement [*Satyawali et al.*, 2009]; adding these microstructural parameters to such a characterization may improve the accuracy. The advantage of using parameters from this physics-based inversion is that they make sense physically based on the known properties of different snow types.

6.2. Derived Micromechanical Parameters

[56] Figure 12 (bottom) shows the strain at failure:

$$\varepsilon_f = \frac{\delta}{L} \tag{19}$$

All four alpine samples have very different values of ε_f, with precipitation particles (B1) showing the most deformation before failure (more than 60%), followed by the rounded grains (B2), then the depth hoar (B3); the brittle sun crust (B4) shows the least strain before failure, as expected. The Alaskan snow samples show much smaller values of strain in the rounded grains (A1) and the depth hoar (A2 and A3), which is not surprising given the much larger temperature gradients in this environment. This indicates that the qualitative descriptions of snow types can be limited when comparing snow from different environments.

[57] The microscale elastic modulus, E_{micro} (equation (11)), and the microscale strength, σ_{micro} (equation (12)), are shown in Figure 13. Figure 13 (top) shows the elastic modulus, and Figure 13 (bottom) shows the strength. For the Alaskan samples, the values of E_{micro} are largest for the refrozen depth hoar (A2), followed by the wind packed snow (A4) and rounded grains (A1), and smallest for the depth hoar (A3). The alpine snow samples show a similar trend, with the sun crust (B4) having the largest values of E_{micro}, followed by the rounded grains (B2), then the depth hoar (B3), and finally the precipitation particles (B1). The microscale elastic modulus, E_{micro}, which is a parameter that is independent of the SMP properties and is useful from an engineering standpoint, has a trend that makes physical sense for all eight snow samples.

[58] The microscale strength (Figure 13, bottom), σ_{micro}, shows the strongest values for the wind packed snow (sample A4), the sun crust (sample B4) and refrozen depth hoar (sample A2), followed by the rounded grains (samples A1 and B2) and depth hoar samples (A3 and B3). Finally the lowest values were measured in the precipitation particles (B1). The microscale strength, σ_{micro}, , which is also a very useful engineering parameter and is independent of the properties of the SMP, also has a trend that makes physical sense for all eight snow samples.

[59] These micromechanical properties are also well separated and have different trends for each property over the eight snow types; the different trends indicate that the properties are not correlated and therefore can be used in combination to characterize snow type. It appears that the samples from the *Johnson and Schneebeli* [1999] study, which were taken in an Alaskan environment, have very different properties than the other four snow types, which were measured in an alpine environment. The snow in

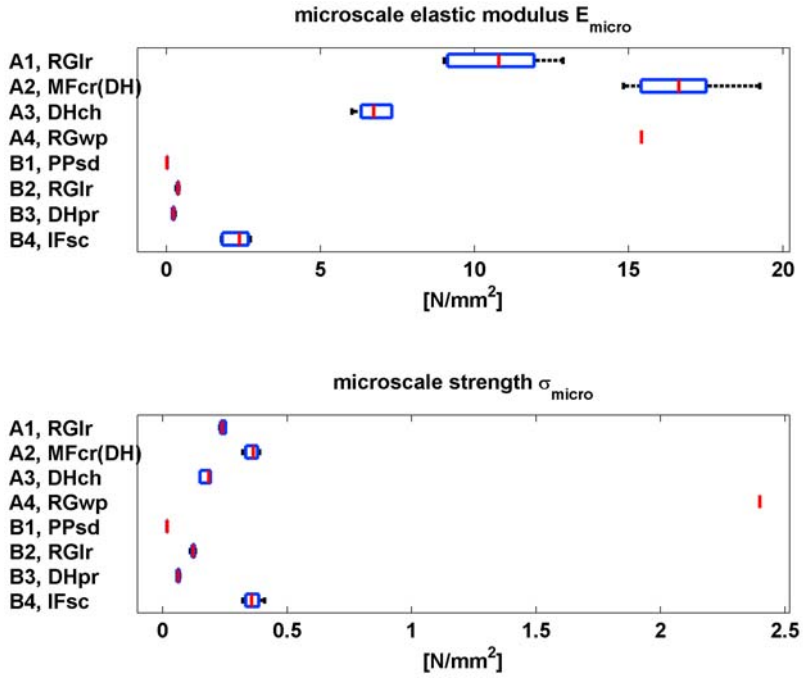

Figure 13. Box plots of (top) microscale elastic modulus, E_{micro}, and (bottom) microscale strength, σ_{micro}, for all eight snow samples. Details of each snow type are given in Table 1. The box shows the middle 50% of the data, the whiskers show 95%, and the plus symbols are outliers.

Alaska is subject to much colder temperatures, much larger temperature gradients, and more extreme maritime conditions, therefore this is not at all surprising since the metamorphism in these two environments is very different.

6.3. Macroscale Strength Estimates

[60] Although the microscale estimates of strength and elastic modulus provide a way to characterize snow type, to apply these estimates to problems at larger scales, microscale quantities must be converted to macroscale values. The macroscale strength is controlled by the number of engaged elements, and can be estimated as [*Johnson and Schneebeli*, 1999]

$$\sigma_{macro} = \sigma_{micro} P_c = \frac{f}{L^2}\frac{\delta}{L} = \frac{f\delta}{V_e} \tag{20}$$

Macroscale strength estimates were calculated for 33 different snow samples, covering a wide range of densities. These values are shown in Figure 14 (left) as a function of density (circles) along with the range of snow strengths measured in previous studies (in gray), from the extensive review by *Shapiro et al.* [1997]. The vertical error bars indicate the range of these estimates within each sample and the horizontal error bars indicate the estimated uncertainty in the density measurements (±5%).

[61] It should also be noted that the values of snow strength reported in the literature were typically performed on sieved snow, in order to provide a nearly homogenous sample. Laboratory strength tests are also rarely performed on depth hoar samples, due to the difficulty in sample collection and testing, and are therefore usually performed on nonfaceted sieved snow which has significantly different mechanical properties. The SMP results, in contrast, include natural dendritic, faceted, and refrozen snow.

[62] Three of the 33 points have error bars that lie completely outside the range of previously reported values. One of these samples had more than 55 ruptures mm^{-1}, and therefore the estimate of structural element length L (and therefore strength) is highly uncertain since the value of L is nonunique (see Figure 4). The other two outliers come from two separate SMP measurements of a highly variable depth hoar layer which, along a 10-m transect, had a measured density range of 197–286 kg m^{-3}. Since both the SMP measurement and the independent density measurement are destructive, these two measurements cannot be made in exactly the same location, and therefore true spatial variability of natural snow may be the cause.

[63] In Figure 14 (right), the x axis is the density as estimated from the SMP hardness measurement directly [*Pielmeier*, 1998; *Marshall*, 2005]. The algorithm used to calculated density was derived from the total penetration force, using a wide range of snow types which may partly explain the larger uncertainty in these estimates (±45 kg m^{-3}). Density should be related to total force (a proxy for strength), however there is likely a different relationship for each snow structure type. Developing density algorithms for each of the primary snow types, and using microscale parameters to identify snow type might improve the accuracy of SMP derived density. This will be investigated in future work.

[64] Although this estimate has a much larger uncertainty, we can be certain that both the density and strength estimates are from exactly the same snow sample. Note that the strength is calculated from the rupture force (based on the variation of signal) and structural element length

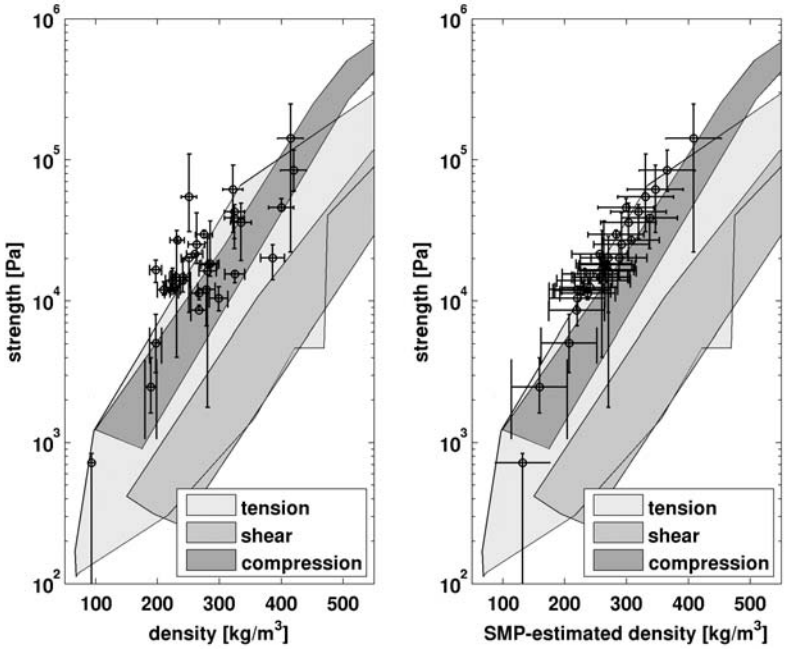

Figure 14. Macroscale strength estimates, σ_{macro}, for 33 different snow samples covering a wide range of densities. The light gray shaded area shows the range of literature values for strength tests performed in tension, the medium gray area shows the range of reported values for shear strength, and the dark gray area shows the range of values for compression tests [*Shapiro et al.*, 1997]. The circles show the SMP estimates of macroscale strength, and the error bars indicate the range of estimates within each sample. (left) Strength estimates as a function of independent direct measurements of density, including the estimated uncertainty in the density measurements (±5%). (right) Strength estimates as a function of density estimated from the median SMP penetration force, with the corresponding estimated uncertainty (±45 kg m^{-3}).

(based on the frequency of the signal), while the density is calculated from the total force. This plot shows better agreement with previously reported values, but has the disadvantage that the density and strength estimates are not completely independent, although they are calculated from very different aspects of the signal.

[65] These values agree reasonably well with results from macroscale tests reported in the literature, especially since there are no "tunable" parameters in this analysis. The only decision that must be made in the above analysis is the noise removal procedure. The rupture force threshold used to remove noise was chosen based on the results of SMP measurements in air. This was done to keep the noise removal objective, since our only estimate of the noise level is from measurements before the SMP tip enters the snow. More sophisticated noise removal procedures could be developed, and if independent measurements of mechanical properties or microstructure were available, this step of the analysis could be improved.

[66] It is interesting to note that the SMP results lie primarily in the range of compressive strength values, which is also at the upper end of the range of previously measured tensile strengths and is an order of magnitude larger than the shear strength values in the literature. The SMP measurement is an indentation test, and therefore this is not surprising. In laboratory compression tests, samples often fail in shear and other modes, however reported values of compression strength are given as the stress required for a sample to fail when loaded in compression, regardless of the actual failure mechanism. In the same manner, in this SMP analysis we do not specifically model the type of failure of individual elements, which likely occurs in bending, tension, and shear. We therefore refer to the SMP derived strength without specifying the exact mode of failure. The trend in SMP estimates of strength as a function of density is similar to that of previously reported measurements of compressive and tensile strength. We could have improved the agreement between our estimates and those previously reported by including an arbitrary offset, however we chose not to do so in order to avoid having any tunable parameters in this algorithm. This potential offset could be due to an effect of the shape of the SMP tip.

[67] Previous attempts at estimating the macroscale elastic modulus E_{macro} have found the resulting values to be 2 orders of magnitude lower than those in the literature, when compared as a function of density. This may be due to the assumption of an isotropic structural element shape. The frequency of rupture events in the SMP signal gives an estimate of the structural element volume, however the isotropic element shape assumption must be employed to estimate the structural element length, L (equation (2) or (3)). Resolving this problem of estimating the macroscale elastic modulus from SMP measurements will be the subject of future work.

[68] If we remove the assumption of an isotropic structural element shape, the macroscale strength (equation (20)) can be expressed as

$$\sigma_{macro} = \sigma_{micro} P_c = \frac{f}{A_s}\frac{\delta}{L} = \frac{f\delta}{V_e} \tag{21}$$

where A_s is the cross-sectional area of the structural element in the plane parallel to the SMP tip, L is the structural element length perpendicular to the SMP tip as before, and $V_e = A_s L$ is the structural element volume. This final form is identical to equation (20).

[69] The macroscale strength, σ_{macro}, therefore, depends only on the structural element volume V_e, rather than on the structural element length L. The structural elements were assumed by *Johnson and Schneebeli* [1999] to have a cubical shape, and by *Sturm et al.* [2004] to have a spherical shape, in order to estimate the structural element length, L, from the volume, V_e. The macroscale strength estimate (equation (21)), however, does not assume any specific shape of the structural elements.

7. Conclusions

[70] Measurements of snow using the SnowMicroPenetrometer show detail at many different scales. The resolution of this instrument allows interpretation of the measurement in the context of microstructural and micromechanical properties of snow. A physical snow penetration theory was first developed by *Johnson and Schneebeli* [1999] with subsequent modifications by *Sturm et al.* [2004], *Kronholm* [2004], and *Marshall* [2005], however most SMP studies have focused on the statistical properties of the direct hardness measurements.

[71] In this paper the original and modified physical snow penetration theories were rigorously tested, using Monte-Carlo simulations over a wide range of microstructural parameters, revealing that in many situations the theories caused large inaccuracies and the predictions were largely biased. Four major sources of error were determined and a new inversion algorithm was developed and introduced to the theory which corrected these problems. The new algorithm was tested over the entire range of parameters observed in snow and was found to recover all the parameters with a much higher accuracy: errors in retrievals are less than 5% in almost all situations, and less than 2% on average, compared with errors of up to 50% using the previous methods.

[72] This new unbiased method was applied to measurements of eight different types of snow from both Alaskan and alpine environments. The structural element length L agreed well with our qualitative understanding of the frequency of bonds in these different snow types. Because the connectivity of snow grains via bonds is important for remote sensing of snow and avalanche forecasting, this parameter may prove to be useful, especially since visual observations of grains and bonds are time consuming and highly subjective. The microscale mechanical parameters showed patterns that made sense physically when compared to the qualitative descriptions of the eight types of snow. This indicates that these micromechanical parameters (e.g., E_{micro}, σ_{micro}) may be very useful from an engineering and slope stability perspective.

[73] The macroscale strength, σ_{macro}, estimated from SMP measurements of 33 different snow types, spanning a wide range of densities, agreed well with previously reported values, without introducing any adjustable parameters into the theory. The macroscale strength estimate does not require an assumption of the geometry of the structural elements (however there may be some dependence on the shape of the penetrometer tip since it is a curved surface). In contrast, estimating the macroscale elastic modulus does require an assumption of the element shape, which may be partially responsible for macroscale elastic modulus estimates not agreeing with literature values in previous work. The scaling of elastic modulus values from the microscale to the macroscale will be the subject of future work.

[74] The resulting microstructural and micromechanical properties for different snow types are significantly different and have very different trends, indicating that a snow characterization may be possible from SMP signals using these physically based estimates. Although this is beyond the scope of this paper, it is hoped that the inversion algorithm described here (code available from the authors upon request) will help standardize processing of SMP measurements. There are more than 15 SMP instruments in use worldwide in the snow science community today, therefore if the SMP analysis procedure can be standardized, then results from different studies around the world can be directly compared. This inversion algorithm will hopefully form a solid foundation upon which a snow characterization, as well as a method for scaling micromechanical properties to scales of importance for engineering and avalanche forecasting, can be built upon in the future. The code used to process the raw SMP data presented in this paper can be downloaded at http://cgiss.boisestate.edu/~hpm/software, or can be obtained by request from the corresponding author (hpm@cgiss.boisestate.edu).

Notation

A	cross-sectional area of SMP tip.
A_s	cross-sectional area of structural element in plane parallel to SMP tip.
d	distance normal to SMP tip.
d_z	distance in vertical direction.
E_{micro}	microscale elastic modulus.
f	rupture force (mean) normal to tip.
f_i	ith individual rupture force normal to tip.
F	force normal to SMP tip.
F_m	mean total force normal to tip.
F_s	SMP sample frequency.
F_z	measured force, in vertical direction.
L	structural element length.
N	number of ruptures.
N_a	number of available elements.
N_e	number of engaged elements.
N_m	number of measured ruptures per mm.
P_c	probability of contact.
r	radius of SMP tip.
V_e	volume of individual structural element.
V_T	total volume displaced during measurement.
z	vertical distance during measurement.

δ deflection at rupture.
ε_f strain at failure.
Δd_i distance from current peak to the ith next peak.
μ coefficient of friction between ice and SMP tip.
θ half angle of SMP tip.
σ_{micro} microscale strength.
σ_{macro} macroscale strength.

[75] **Acknowledgments.** This manuscript was significantly improved by the suggestions of Martin Schneebeli and two anonymous reviewers.

References

Birkeland, K., K. Kronholm, M. Schneebeli, and C. Pielmeier (2004), Changes in the shear strength and micro-penetration hardness of a buried surface-hoar layer, *Ann. Glaciol.*, *38*, 223–228, doi:10.3189/172756404781815167.

Colbeck, S. C., and E. A. Anderson (1982), The permeability of a melting snow cover, *Water Resour. Res.*, *18*(4), 904–908, doi:10.1029/WR018i004p00904.

Dadic, R., M. Schneebeli, M. Lehning, M. A. Hutterli, and A. Ohmura (2008), Impact of the microstructure of snow on its temperature: A model validation with measurements from Summit, Greenland, *J. Geophys. Res.*, *113*, D14303, doi:10.1029/2007JD009562.

Fierz, C., R. L. Armstrong, Y. Durand, P. Etchevers, E. Greene, D. M. McClung, K. Nishimura, P. K. Satyawali, and S. A. Sokratov (2009), *The International Classification for Seasonal Snow on the Ground*, *IHP Tech. Doc. in Hydrol. Ser.*, UNESCO-IHP, Paris, in press.

Flin, F., J. B. Brzoska, B. Lesaffre, C. Cileou, and R. A. Pieritz (2003), Full three-dimensional modelling of curvature-dependent snow metamorphism: First results and comparison with experimental tomographic data, *J. Phys. D Appl. Phys.*, *36*, *10A*, A49–A54, doi:10.1088/0022-3727/36/10A/310.

Gibson, L. J., and M. F. Ashby (1997), *Cellular Solids: Structure and Properties*, 2nd ed., 510, pp., Cambridge Univ. Press, Cambridge, U. K.

Johnson, J. B., and M. Schneebeli (1999), Characterizing the microstructural and micromechanical properties of snow, *Cold Reg. Sci. Technol.*, *30*, 91–100, doi:10.1016/S0165-232X(99)00013-0.

Kaempfer, T. U., and M. Schneebeli (2007), Observation of isothermal metamorphism of new snow and interpretation as a sintering process, *J. Geophys. Res.*, *112*, D24101, doi:10.1029/2007JD009047.

Kirchner, H. O. K., G. Michot, H. Narita, and T. Suzuki (2001), Snow as a foam of ice: Plasticity, fracture and the brittle-to-ductile transition, *Philos. Mag. A*, *81*(9), 2161–2181, doi:10.1080/01418610108217141.

Kronholm, K. (2004), Spatial variability of snow mechanical properties with regard to avalanche formation, Ph.D. thesis, 218 pp., Univ. of Zurich, Zurich, Switzerland.

Kronholm, K., M. Schneebeli, and J. Schweizer (2004), Spatial variability of micropenetration resistance in snow layers on a small slope, *Ann. Glaciol.*, *38*, 202–208, doi:10.3189/172756404781815257.

Lundmark, C. L., and J. P. Ball (2008), Living in snowy environments: Quantifying the influence of snow on moose behavior, *Arct. Antarct. Alp. Res.*, *40*(1), 111–118, doi:10.1657/1523-0430(06-103)[LUNDMARK]2.0.CO;2.

Lutz, E., K. Birkeland, K. Kronholm, K. Hansen, and R. Aspinall (2007), Surface hoar characteristics derived from a snow micropenetrometer using moving window statistical operations, *Cold Reg. Sci. Technol.*, *47*, 118–133, doi:10.1016/j.coldregions.2006.08.021.

Marshall, H. P. (2005), Snowpack spatial variability: Towards understanding its effect on remote sensing measurements and snow slope stability, Ph.D. thesis, 294 pp., Dep. of Civil Eng., Univ. of Colo. at Boulder, Boulder, Colo.

McClung, D., and P. Schaerer (1993), *The Avalanche Handbook*, 1st ed., edited by L. Gunnarson, Mountaineers Books, Seattle, Wash.

Nemat-Nasser, S., and M. Hori (1999), *Micromechanics: Overall Properties of Heterogeneous Materials*, 2nd ed., 786 pp., Elsevier, Amsterdam.

Petrovic, J. J. (2003), Mechanical properties of ice and snow: Review, *J. Mater. Sci.*, *38*, 1–6, doi:10.1023/A:1021134128038.

Pielmeier, C. (1998), Analysis and discrimination of snow structure and snow profiles using a high resolution penetrometer, Diploma thesis, 123 pp., Ludwig-Maximilians-Univ., Munich, Germany.

Pielmeier, C. (2003), Textural and mechanical variability of mountain snowpacks, Ph.D. thesis, 127, pp. Universität Bern, Bern, Switzerland.

Pielmeier, C., and M. Schneebeli (2003), Stratigraphy and changes in hardness of snow measured by hand, ramsonde and snow micro penetrometer: A comparison with planar sections, *Cold Reg. Sci. Technol.*, *37*, 393–405, doi:10.1016/S0165-232X(03)00079-X.

Rees, W. G. (2006), *Remote Sensing of Snow and Ice*, 285, pp. Taylor and Francis, Boca Raton, Fla.

Satyawali, P. K., M. Schneebeli, C. Pielmeier, T. Stucki, and A. K. Singh (2009), Preliminary characterization of alpine snow using SnowMicroPen, *Cold Reg. Sci. Technol.*, *55*, 311–320, doi:10.1016/j.coldregions.2008.09.003.

Schneebeli, M., and J. B. Johnson (1998), A constant-speed penetrometer for high-resolution snow stratigraphy, *Ann. Glaciol.*, *26*, 107–111.

Schneebeli, M., C. Pielmeier, and J. B. Johnson (1999), Measuring snow microstructure and hardness using a high resolution penetrometer, *Cold Reg. Sci. Technol.*, *30*, 101–114, doi:10.1016/S0165-232X(99)00030-0.

Schweizer, J., B. Jamieson, and M. Schneebeli (2003), Snow avalanche formation, *Rev. Geophys.*, *41*(4), 1016, doi:10.1029/2002RG000123.

Shapiro, L. H., J. B. Johnson, M. Sturm, and G. L. Blaisdell (1997), Snow mechanics: Review of the state of knowledge and applications, *Tech. Rep. 97–3*, Cold Reg. Res. Eng. Lab., Hanover, N. H.

Sturm, M., J. B. Johnson, and J. A. Holmgren (2004), Variations in the mechanical properties of Arctic and subarctic snow at local (1-m) to regional scales (100-km), paper presented at International Symposium on Snow Monitoring and Avalanches, pp. 233–244, Snow and Avalanche Study Estab., Manali, India, 12–16 Apr.

J. B. Johnson, Institute of Northern Engineering, University of Alaska Fairbanks, P.O. Box 755910, Fairbanks, AK 99775-5910, USA.

H.-P. Marshall, Center for Geophysical Investigation of the Shallow Subsurface, Department of Geosciences, Boise State University, 1910 University Drive, MG206E, Boise, ID 83725, USA. (hpm@cgiss.boisestate.edu)